

Deformation behaviours of SS304 tubes in pulsating hydroforming processes

Lianfa Yang*, Ninghua Wang and Yulin He

Faculty of Mechanical & Electrical Engineering, Guilin University of Electronic Technology,
Guilin 541004, Guangxi, P.R. China

(Received November 17, 2015, Revised May 15, 2016, Accepted July 12, 2016)

Abstract. Tube hydroforming (THF) under pulsating hydraulic pressures is a novel technique that applies pulsating hydraulic pressures that are periodically increased to deform tubular materials. The deformation behaviours of tubes in pulsating THF may differ compared to those in conventional non-pulsating THF due to the pulsating hydraulic pressures. The equivalent stress-strain relationship of metal materials is an ideal way to describe the deformation behaviours of the materials in plastic deformation. In this paper, the equivalent stress-strain relationships of SS304 tubes in pulsating hydroforming are determined based on experiments and simulation of free hydraulic bulging (FHB), and compared with those of SS304 tubes in non-pulsating THF and uniaxial tensile tests (UTT). The effect of the pulsation parameters, including amplitude and frequency, on the equivalent stress-strain relationships is investigated to reveal the plastic deformation behaviours of tubes in pulsating hydroforming. The results show that the deformation behaviours of tubes in pulsating hydroforming can be well described by the equivalent stress-strain relationship obtained by the proposed method. The amplitude and frequency of pulsating hydraulic pressure have distinct effects on the equivalent stress-strain relationships—the equivalent stress becomes augmented and the formability is enhanced with the increase of the pulsation amplitude and frequency.

Keywords: tube hydroforming; pulsating; stress-strain relationship; free hydraulic bulging

1. Introduction

Tube hydroforming (THF) technology is a flexible forming technique used to obtain complex hollow parts using hydraulic pressure as the forming media. THF constitutes a significant manufacturing process approach to the realization of lightweight parts since it offers multiple advantages, such as the low cost of production, low weight, and high strength, as described by (Zhan *et al.* 2010). THF under pulsating hydraulic pressures (pulsating THF) is a novel technique that applies hydraulic pressures P that are periodically increased in a pulsating manner at a certain amplitude and frequency to deform tubular materials. Since the novel technique bears some advantage and potential applications in automobile industry, as stated by Rikimaru (2001) and Loh-Mousavi (2008), some studies have shown that the quality of the hydroformed workpieces could be achieved under lower hydraulic pressures by the pulsating THF. Mori (2007), Loh-

*Corresponding author, Ph.D., E-mail: y-lianfa@163.com

Mousavi (2008), Loh-Mousavi (2010), Loh-Mousavi (2011) compared the deformation behaviour of tubes in pulsating and non-pulsating hydroforming via finite element (FE) simulations and in experimental investigations and found that the formability of the tubes could be considerably improved by the pulsating hydraulic pressures. Xu *et al.* (2014) found that the pulsating hydraulic pressures could promote material feeding and reduce the effect of friction during the hydroforming process. Therefore, better filling ability of materials and increased uniformity of wall thicknesses of workpieces were obtained. Yang *et al.* (2014) investigated the deformation behaviour of tubes in hydroforming with radial crushing under linear and pulsating hydraulic pressures and concluded that a more uniform wall thickness and a higher shape accuracy is achieved, features that have been attributed to a proper pulsating hydraulic pressure.

The equivalent stress-strain relationship ($\sigma_e=f(\varepsilon_e)$), or equivalently the plastic hardening law, is an ideal way to describe the deformation behaviour of the materials in plastic deformation. In THF, the equivalent stress-strain relationship of tubes is essential for the analysis of deformation behaviours, the assessment of the forming limit and the performance of precise FE simulations of the process. The uniaxial tensile test (UTT) is generally applied to determine the equivalent stress-strain relationship of sheet materials. However, direct introduction of the data primarily derived from the UTT into the THF analyses may give rise to an unacceptable discrepancy due to the different stress states, namely, the uniaxial stress state in the UTT and the biaxial stress state in THF (Yang *et al.* 2008). A reasonable choice for determining the equivalent stress-strain relationship of tubes in THF is the free hydraulic bulging (FHB). However, with the FHB method, the instantaneous meridian radii (ρ_ϕ) of the bulged profiles under increasing hydraulic pressures, P , must be directly measured in real time during the entire process of hydroforming. The real-time measurement involves laborious and tedious work (Bortot *et al.* 2008). To avoid such laborious and tedious measurement, the meridian bulged profiles of the tubes were assumed to possess the shape of simple curves for convenient determination of the instantaneous meridian radii (ρ_ϕ), using mathematical derivation methods. For instance, Strano *et al.* (2004) assumed that the outer and inner bulged profiles were cosine curves in order to conveniently determine the equivalent stress-strain relationship of tubes based on the energy balance theory. Yang *et al.* (2008) assumed that the bulged profiles were polynomial curves and were used to determine the equivalent stress-strain relationship based on the force equilibrium equations and the plastic membrane theory. Hwang *et al.* (2009) assumed that the bulged profiles were elliptical curves used to obtain the equivalent stress-strain relationship by adopting Hill's orthogonal anisotropic theory. Boudeau *et al.* (2012) assumed that the bulged profiles were arc curves used to determine the equivalent stress-strain relationship by establishing a complete analytical model combined with the experimental procedure.

In the research studies referred above, the assumed bulged profiles may fail to accurately describe the actual bulged profiles. Moreover, the total strain theory and the proportional loading assumption have been adopted. In fact, it is difficult to implement the proportional loading in THF, especially in pulsating THF-featured pulsating loading. Considering the complexity of the loading way, it is advisable to apply the incremental plasticity theory instead of the total strain theory to address the equivalent stress-strain relationship of the tubes in pulsating hydroforming. In pulsating hydroforming, the deformation behaviours of tubes are affected by the pulsating parameters, such as the pulsation amplitude, ΔP , and the pulsation frequency, f , of the hydraulic pressures, in a potentially more complicated manner than in conventional THF. Very little work has been performed on the determination of the equivalent stress-strain relationship of the tubes in pulsating hydroforming, and on the effect of pulsating parameters on the equivalent stress-strain

relationship.

The aim of this research is to determine the equivalent stress-strain relationship of tubes in pulsating hydroforming and the influence of the pulsating parameters on the equivalent stress-strain relationship. An analytic formula ($\sigma_e=f(\varepsilon_e)$ for the equivalent stress-strain relationship) is first derived on the basis of the incremental plasticity theory, the law of plastic deformation work, and on other factors. The experiments of pulsating and non-pulsating THF were then carried out on SS304 stainless steel tubes using a custom-made THF experimental system to collect the deformation data for quantifying the relationships. The equivalent stress-strain relationships determined based on the data of UTT and FHB experiments and the FE simulations are compared to verify the proposed method. Finally, the effect of the pulsation amplitude, ΔP , and pulsation frequency, f , of the hydraulic pressures on the equivalent stress-strain relationships that are determined based on the experimental data, is investigated to reveal the plastic deformation behaviours of tubes in pulsating hydroforming.

2. Methodologies

As shown in Fig. 1, the procedures used to establish and quantify the equivalent stress-strain relationship, and the analysis method of the effect of pulsating parameters on the relationship, are introduced as follows:

- (1) The expression for the equivalent stress-strain relationship ($\sigma_e=f(\varepsilon_e)$) of tubes in THF is established based on the mechanical model of FHB, the incremental plasticity theory, and the law of plastic deformation work. The formulae for the meridian and circumferential stresses (σ_ϕ and σ_θ) on the bulged profile are derived using the static equilibrium method, with the assumption of $\sigma_r=0$ (i.e., the stress σ_r along the wall-thickness direction is ignored). An approach to determine the instantaneous meridian radii (ρ_ϕ) of arbitrary points on the bulged profiles is then proposed on the basis of the assumption that the axial bulged profiles of the tubes in THF are polynomial curves. The calculation formulae of equivalent strains are given based on the law of constant volume during plastic deforming and the incremental plasticity theory. The formulas for equivalent stress are derived based on the law of plastic deformation work. Finally, the expression for the equivalent stress-strain relationship ($\sigma_e=f(\varepsilon_e)$) of tubes in THF is established based on a polynomial plastic hardening model.
- (2) The FHB experiments under pulsating and non-pulsating hydraulic pressures are performed on SS304 stainless steel tubes on a custom-made THF experimental system to collect the deformation data on the bulged region of tubes for quantifying the equivalent stress-strain relationships. The instantaneous hydraulic pressures during the FHB experiments were recorded in real-time, and the deformation images on the bulged zone of the tubes are captured on-line by a 3D digital image correlation system. The data of the coordinates, axial and circumferential strains, and instantaneous wall thickness of the bulged profiles are extracted from deformation images.
- (3) The equivalent stress-strain curves $\sigma_{p-exp}=f(\varepsilon_{p-exp})$ and $\sigma_{n-exp}=f(\varepsilon_{n-exp})$ of the tubes in pulsating and non-pulsating THF are respectively obtained based on the above experimental deformation data, and were compared with the equivalent stress-strain curve $\sigma_{u-exp}=f(\varepsilon_{u-exp})$ obtained based on the conventional UTT.
- (4) The FE models for FHB under pulsating and non-pulsating pressures are established. The equivalent stress-strain curves $\sigma_{p-exp}=f(\varepsilon_{p-exp})$, $\sigma_{n-exp}=f(\varepsilon_{n-exp})$ and $\sigma_{u-exp}=f(\varepsilon_{u-exp})$ are respectively

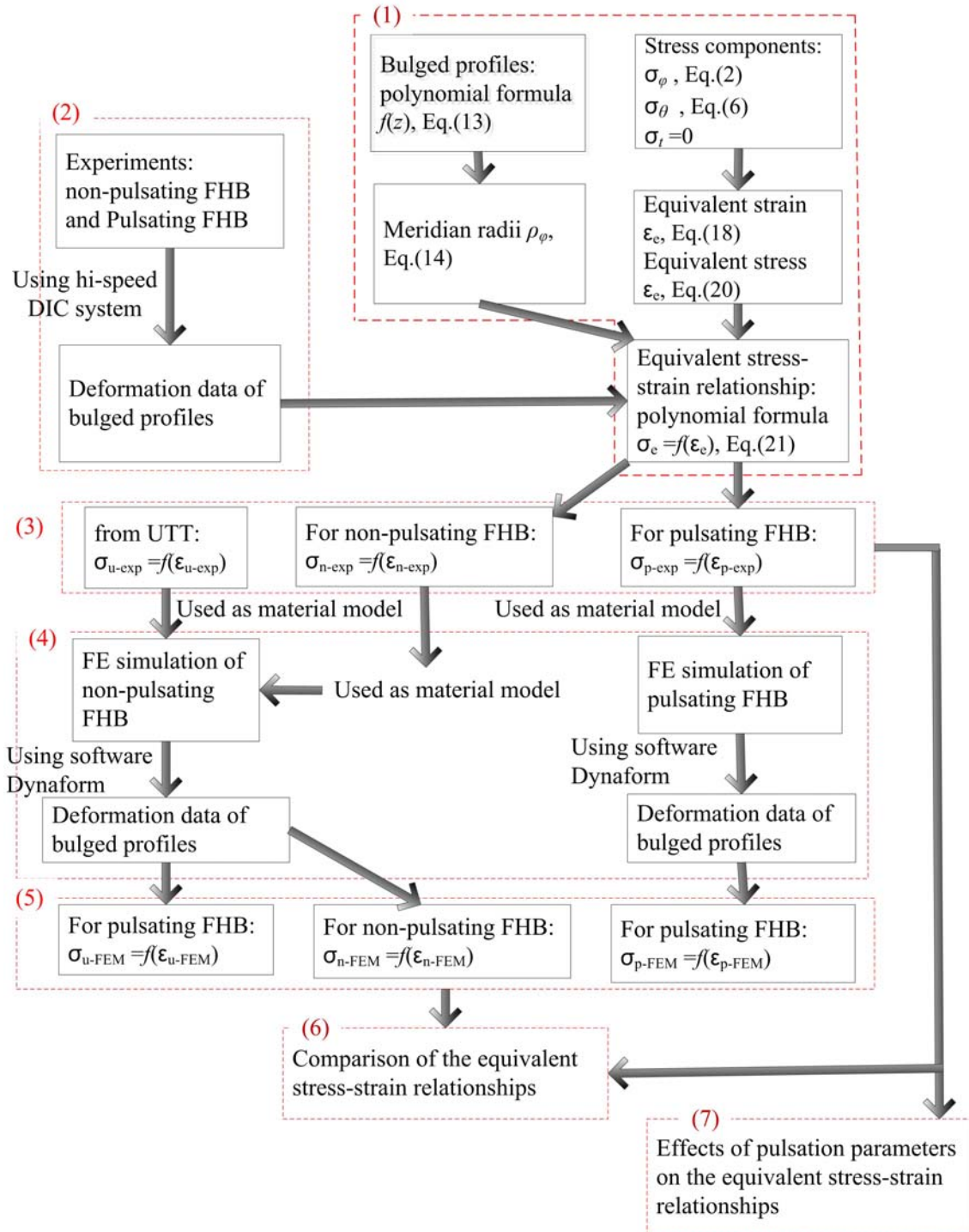


Fig. 1 Flow chart diagram of the procedures used to establish equivalent stress-strain relationships and to analyse the effect of pulsating parameters

input into the models as material models, and the FE simulations of FHB under pulsating and non-pulsating pressures are carried out. Similarly, the data of the coordinates, axial and circumferential strains, and instantaneous wall thickness of the bulged profiles are drawn out from FE simulation results.

(5) Three equivalent stress-strain curves of the form $\sigma_{p-FEM}=f(\varepsilon_{p-FEM})$ under pulsating FHB, and $\sigma_{n-FEM}=f(\varepsilon_{n-FEM})$ and $\sigma_{u-FEM}=f(\varepsilon_{u-FEM})$ under non-pulsating FHB, are obtained by applying the elicited simulation results into the derived equivalent stress-strain relationship $\sigma_e=f(\varepsilon_e)$.

(6) The difference of equivalent stress-strain relationships ($\sigma_{p-exp}=f(\varepsilon_{p-exp})$, $\sigma_{n-exp}=f(\varepsilon_{n-exp})$, and $\sigma_{u-exp}=f(\varepsilon_{u-exp})$) determined based on the FHB experimental data and those relationships ($\sigma_{p-FEM}=f(\varepsilon_{p-FEM})$, $\sigma_{n-FEM}=f(\varepsilon_{n-FEM})$, and $\sigma_{u-FEM}=f(\varepsilon_{u-FEM})$) determined based on the simulation data of non-pulsating and pulsating FHB were used to verify the accuracy of the proposed method in this paper.

(7) The effects of the pulsation amplitude and frequency on the equivalent stress-strain curves determined based on the experimental deformation data are analyzed and the plastic deformation of tubes in the pulsating hydroforming is summarized.

3. Establishment of equivalent stress-strain relationship

In this section, the expression for the equivalent stress-strain relationship ($\sigma_e=f(\varepsilon_e)$) of tubes in FHB is established based on the mechanical model of FHB, the incremental plasticity theory, and the law of plastic deformation work.

3.1 Expressions for meridian stress σ_z and circumferential stress σ_θ

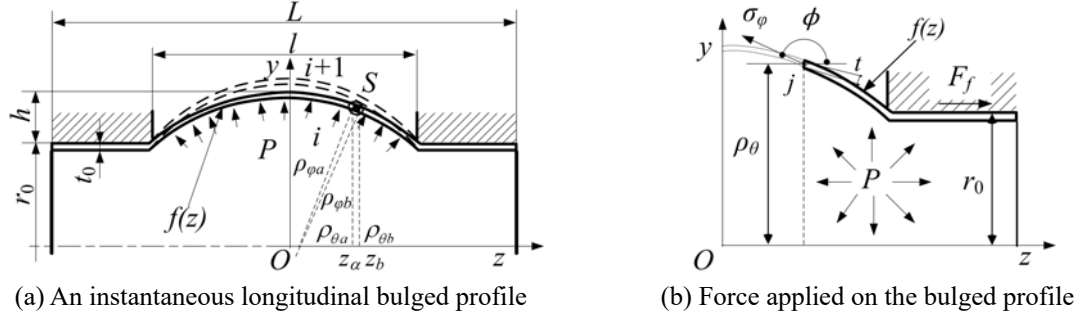
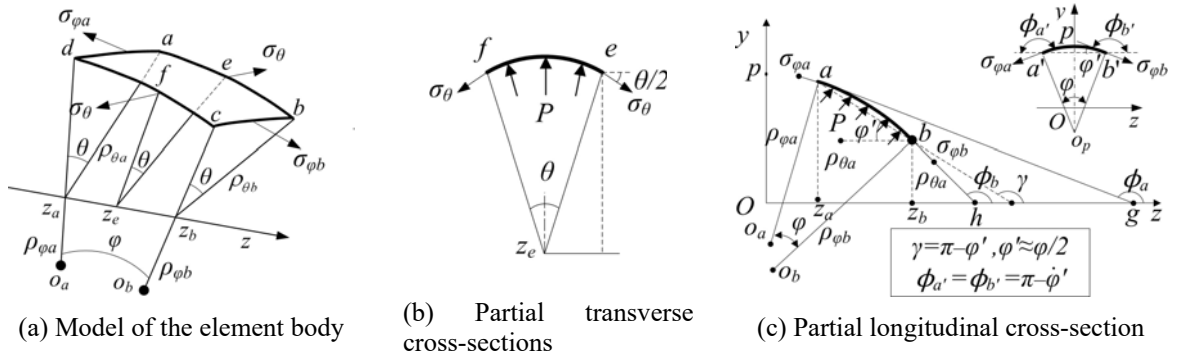
For the sake of a convenient analysis, the following assumptions are postulated with the present method:

- (1) The tubular material is homogeneous, isotropic, and incompressible, and meets the von Mises yield criterion
- (2) The transverse cross-sections of the bulged tubes remain circular, and the longitudinal (axial) cross-section remains axially symmetrical in the process of deformation
- (3) The two ends of the tubes are able to freely shrink in the axial direction in the process of deformation
- (4) The stress σ_t in the wall-thickness direction is ignored, i.e., $\sigma_t=0$, in view of the small ratio of the wall thickness t_0 to the initial outer radius r_0 of tubular blanks
- (5) The meridian stress σ_ϕ , circumferential stress σ_θ , and thickness stress σ_t are the principal stresses
- (6) The bending deformation of the bulged profile is ignored

If any point j is taken on the bulged profile $f(z)$ as an analytical object. Based on the mechanical model of FHB shown in Fig. 2, the following force equilibrium equation on the point j along the z -axis direction can be obtained from Fig. 2(b) as

$$\sigma_\phi 2\pi t(\rho_\theta - t/2) \cos(\pi - \phi) = \pi P(\rho_\theta - t)^2 - F_j \quad (1)$$

The meridian stress σ_ϕ of an arbitrary point on the bulged profile can be written in accordance to Eq. (1).

Fig. 2 Schematic of a tube in free hydraulic bulging under hydraulic pressure P Fig. 3 Mechanical model of an infinitesimal element S on the bulged profile under hydraulic pressure P

$$\sigma_{\varphi} = \frac{P(\rho_{\theta} - t)^2 - F_f}{2t(\rho_{\theta} - t/2)\cos(\pi - \phi)} \quad (2)$$

The friction between the tube and dies shown in Fig. 1(b) can be calculated using the following equation

$$F_f = \mu P \pi r_0 (L - l) \quad (3)$$

As shown in Fig. 3(a), an infinitesimal element S on the bulged profile is selected for analysing the force conditions of the bulged tube. The element S has planar symmetry along the y - z plane, spans a meridian angle φ , and a circumferential angle θ , eliciting the following results $\rho_{\theta a} = \rho_{\theta d}$, $\rho_{\theta b} = \rho_{\theta c}$, $ab_{in} = cd_{in}$, $ad_{in} > bc_{in}$. Consequently, the edge lengths of the element body S can be calculated using the following equations

$$\begin{aligned} ad_{mid} &= (\rho_{\theta a} - t_a/2)\sin\theta \\ bc_{mid} &= (\rho_{\theta b} - t_b/2)\sin\theta \\ ad_{mid} = cd_{mid} &= (\rho_{\theta b} - t_p/2)\sin\varphi \\ ad_{in} &= (\rho_{\theta a} - t_a)\sin\theta \\ bc_{in} &= (\rho_{\theta b} - t_b)\sin\theta \\ ab_{in} = cd_{mid} &= (\rho_{\theta} - t_p)\sin\varphi \end{aligned} \quad (4)$$

According to Fig. 3(b) and Fig. 3(c), the force equilibrium equation in the y -axis direction for the element body S can be written as.

$$2\sigma_{\theta}ab_{mid}t_p \sin \frac{\theta}{2} + \sigma_{\phi a}ad_{mid}t_a \sin(\phi_a) + \sigma_{\phi b}bc_{mid}t_b \sin(\phi_b) = p \frac{1}{2}(ad_{in} + bc_{in})ab_{in}|\cos \gamma| \quad (5)$$

For an infinitesimal element S , the formulas $\sin\theta=\theta$, $\sin(\theta/2)=\theta/2$ hold true. By substituting Eqs. (2)-(4) into Eq. (5), the circumferential stress σ_{θ} can be derived as

$$\sigma_{\theta} = \frac{\left\{ \begin{array}{l} P[(\rho_{\theta a} - t_a) + (\rho_{\theta b} - t_b)] \times (\rho_{\phi} - t_p) \sin \varphi \cos(\pi - \phi) |\cos \gamma| \\ - [P(\rho_{\theta a} - t_a)^2 - F_f] \sin \phi_a - [P(\rho_{\theta b} - t_b)^2 - F_f] \sin \phi_b \end{array} \right\}}{2t_p(\rho_{\phi} - t_p / 2) \sin \varphi \cos(\pi - \phi)} \quad (6)$$

If the peak point p is taken on the bulged profile as an analytical object. For the infinitesimal element at the peak p , the infinitesimal bulged profile appears horizontal, and the two endpoints a' and b' are symmetrical relative to the y -axis, as shown in Fig. 3(c). Consequently, the deformation data of the two endpoints are identical, and the formulas $\rho_{\phi a}=\rho_{\phi b}=\rho_{\phi p}$, $\rho_{\theta a}=\rho_{\theta b}\approx\rho_{\theta p}$, $t_p=t_a\approx t_b$, and $\phi_a=\phi_b\approx\pi-\varphi/2$ hold true. Moreover, in view of the conditions $\sin\varphi=\varphi$, $\sin(\varphi/2)=\varphi/2$, $\gamma=\pi$, and $\cos(\pi-\phi)\approx 1$, Eq. (6) can be rewritten as

$$\sigma_{\theta} = \frac{2P(\rho_{\theta} - t_p) \times (\rho_{\phi} - t_p) - [P(\rho_{\theta} - t_p)^2 - F_f]}{2t_p(\rho_{\phi} - t_p / 2)} \quad (7)$$

When the frictional force F_f is ignored, the meridian stress σ_{ϕ} at the peak p can be derived from Eq. (2) as

$$\sigma_{\phi} = \frac{P(\rho_{\theta} - t_p)^2}{2t_p(\rho_{\theta} - t_p / 2)} \quad (8)$$

From Eq. (7), the circumferential stress σ_{θ} at the peak p on the bulged profile can be obtained as

$$\sigma_{\theta} = \frac{P(\rho_{\theta} - t_p / 2)}{t_p} \left[\left(1 - \frac{t_p}{2(\rho_{\phi} - t_p / 2)} \right) \left(1 - \frac{t_p}{2(\rho_{\theta} - t_p / 2)} \right) - \frac{(\rho_{\theta} - t_p)^2}{2(\rho_{\theta} - t_p / 2)(\rho_{\phi} - t_p / 2)} \right] \quad (9)$$

Both Eq. (8) and Eq. (9) derived for calculating the meridian and circumferential stresses at the peak of the bulged profiles are identical to those derived by Fuchizawa *et al.*(1993).

3.2 Determination of longitudinal profiles of bulged tube

According to Eqs. (2) and (7), the determination of the meridian radius ρ_{ϕ} of the selected point on the bulged profile is a prerequisite for the calculation of the meridian and circumferential stresses (σ_{ϕ} and σ_{θ}).

It is tedious and impractical to directly measure the instantaneous meridian radius ρ_{ϕ} during the FHB experiments. Thus, the following procedures are adopted in the present research. After the 3D displacement fields of the bulged tubes were measured with the use of the hi-speed 3D digital image correlation (DIC) system (hereinafter referred to as hi-speed DIC system) in real-time

during the entire FHB process, the 3D geometrical models of the bugled zone at each time step were rebuilt with the 3D displacement field data. The coordinate data (z, y) of the longitudinal (axial) cross-section were then extracted at regular intervals along the z -axis from the 3D geometrical models. Next, the following polynomial functions $y=f(z)$ were introduced to express the bulged profiles by fitting the coordinate data.

$$f(z) = a_0 + a_1z + a_2z^2 + a_3z^3 + a_4z^4 \cdots \quad (10)$$

Finally, the meridian radius ρ_ϕ of the selected point on the bulged profiles can be respectively calculated by

$$\rho_\phi = \left| \frac{[1+f'(z)^2]^{3/2}}{f''(z)} \right| \quad (11)$$

3.3 Expressions of the equivalent strain and stress relationship

The meridian and circumferential strains at each time step were obtained by the hi-speed DIC in the FHB experiments. Consequently, according to the assumption of incompressible materials, the thickness strain ε_t at each time step can be calculated by

$$\varepsilon_t = -\varepsilon_\theta - \varepsilon_\phi \quad (12)$$

Therefore, the strain increments at each time step can be calculated by

$$\begin{aligned} d\varepsilon_{\theta(i)} &= \varepsilon_{\theta(i)} - \varepsilon_{\theta(i-1)} \\ d\varepsilon_{\phi(i)} &= \varepsilon_{\phi(i)} - \varepsilon_{\phi(i-1)} \\ d\varepsilon_{t(i)} &= \varepsilon_{t(i)} - \varepsilon_{t(i-1)} \end{aligned} \quad (13)$$

According to the incremental Levy-Mises constitutive relation, the equivalent strain increment $d\varepsilon_e$ at each time step in the FHB is calculated by

$$d\varepsilon_{e(i)} = \frac{\sqrt{2}}{3} \sqrt{(d\varepsilon_{\theta(i)} - d\varepsilon_{\phi(i)})^2 + (d\varepsilon_{\phi(i)} - d\varepsilon_{t(i)})^2 + (d\varepsilon_{t(i)} - d\varepsilon_{\theta(i)})^2} \quad (14)$$

The equivalent strain ε_e at each time step in the FHB can be obtained by cumulating the equivalent strain increment $d\varepsilon_e$ in the entire FHB process.

$$\varepsilon_{e(i)} = \sum_{i=1}^m (d\varepsilon_{e(i)}) \quad (15)$$

On the other hand, based on the law of plastic deformation work, the equivalent stress σ_e can be determined by (Hosford *et al.* 2011)

$$\sigma_{e(i)} d\varepsilon_{e(i)} = \sigma_{\theta(i)} d\varepsilon_{\theta(i)} + \sigma_{\phi(i)} d\varepsilon_{\phi(i)} + \sigma_{t(i)} d\varepsilon_{t(i)} \quad (16)$$

In view of the assumption of $\sigma_r=0$ in the present analysis, the equivalent stress at each time step in the FHB process is expressed by

$$\sigma_{e(i)} = \left(\sigma_{\theta(i)} d\varepsilon_{\theta(i)} + \sigma_{\phi(i)} d\varepsilon_{\phi(i)} \right) / d\varepsilon_{e(i)} \quad (17)$$

The Hollomon formula $\sigma = K\varepsilon_e^n$ and the Krupkowsky formula $\sigma = K(\varepsilon_\theta + \varepsilon_e)^n$ are generally used to describe the equivalent stress-strain relationship. The authors found earlier that the polynomial formula can precisely represent the equivalent stress-strain relationship of SS304 stainless steel tubes (Jia *et al.*, 2014). Accordingly, the following polynomial formula is adopted to represent the equivalent stress-strain relationship in this paper.

$$\sigma_e = f(\varepsilon_e) = \lambda_0 + \lambda_1 \varepsilon_e^1 + \lambda_2 \varepsilon_e^2 + \lambda_3 \varepsilon_e^3 + \lambda_4 \varepsilon_e^4 + \dots \quad (18)$$

4. Experiments of free hydraulic bulging

According to the previous section, in order to determine the equivalent stress-strain relationship, the following variables at the peak p on the axial bulged profiles at each forming step during THF must be determined in advance, including the hydraulic pressure P , wall thickness t , axial strain increment $d\varepsilon_\theta$, circumferential strain increment $d\varepsilon_\phi$, coordinates of points on the axial bulged profiles, etc. These data are obtained from FHB experiments by the custom-made THF experimental system. This system is briefly introduced below.

4.1 Configuration of the THF experimental system

As shown in Fig. 4, the custom-made THF experimental system comprises a hydraulic power generation system, a pulsation generation system, a free hydraulic bulging device and a hi-speed DIC system. With the custom-made THF system, both the non-pulsating and the pulsating FHB can be performed.

(1) **Hydraulic power generation system.** The main part of the system is an electric pressure-testing pump in which the fluid experiences a monotonically increasing hydraulic pressure P_0 (as indicated in Fig. 5). The fluid is then led into the pulsation generation system. The maximum hydraulic pressure for the bulging can be preset by an overflow valve installed in the system.

(2) **Pulsation generation system.** This system is composed of a mini-servo press, a hydraulic chamber, and a piston rod. The hydraulic chamber is installed on the working table of the servo press. One end of the piston rod is fixed onto the sliding block of the servo press, while the other end is inserted into the hydraulic chamber. The cyclic upward and downward movement of the piston rod with the sliding block drives the fluid in the hydraulic chamber in a pulsating manner, generating a pulsating hydraulic pressure $P = P_0 + \Delta P \sin(2\pi fT)$, as shown in Fig. 5. The pulsating hydraulic fluid is then supplied to the tubular blank on the free hydraulic bulging device. The pulsation frequency and amplitude of the hydraulic pressure can be controlled by changing the stroke and speed of the slider on the control panel of the servo press.

(3) **Free hydraulic bulging device (FHB device).** This device is mainly made up of two locating rings, two urethane plugs and a hollow bolt, as shown in Fig. 6. Two urethane plugs were placed into the tubular blank, which were then inserted into the locating rings at the two ends. The tubular blank, locating rings, and urethane plugs were fixed together by the hollow bolt to create an initial sealing. Fluid was led into the device through the hollow bolt, and the

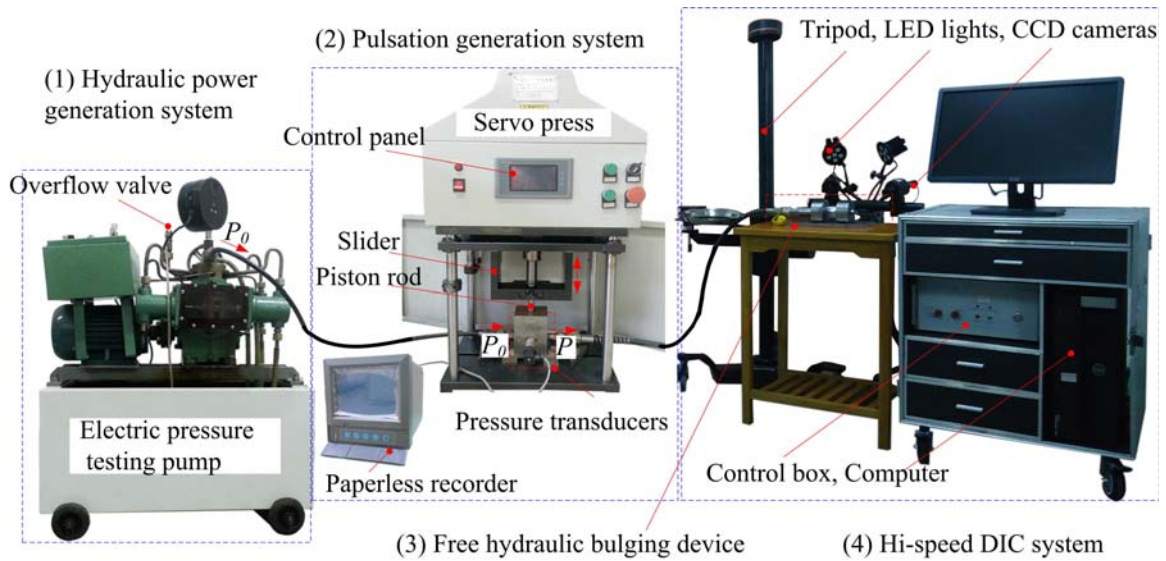


Fig. 4 Configuration of custom-made tube hydroforming (THF) experimental system with pulsating hydraulic pressure

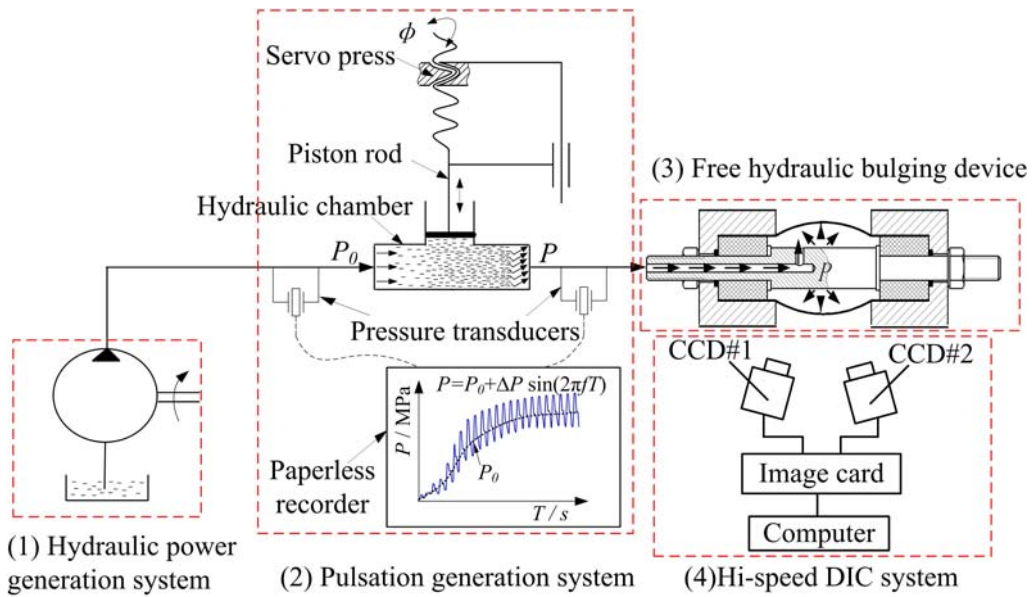


Fig. 5 Schematic diagram of the working principle of the pulsation generation system

hydraulic pressure inside the tubular blank was thus increased. The urethane plugs were then expanded and pressed the tubular blank against the internal surfaces of the locating rings, thereby generating a strong sealing. The two ends of the tubular blank could freely shrink to some degree in the axial direction despite the friction between the tubular blank and the locating rings, thus generating FHB. Considering the friction between the tube and the locating rings and the urethane plugs, Eq. (3) should be amended as

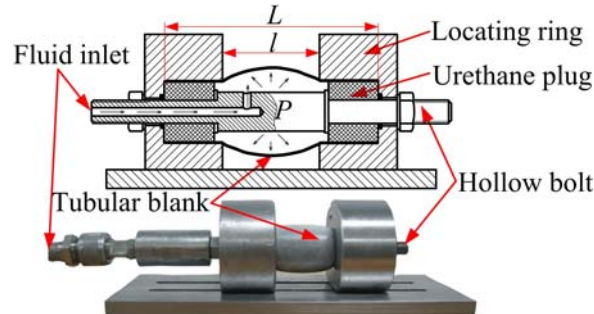


Fig. 6 Schematic and photograph of the free hydraulic bulging device used in the experiments conducted in this study

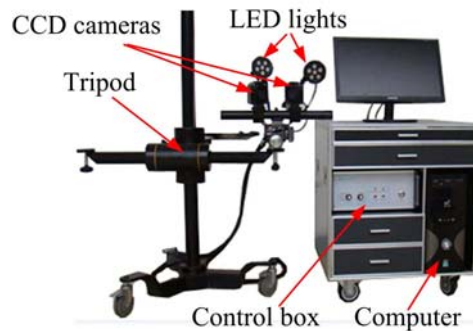


Fig. 7 Hi-speed DIC system used for the recording of 3D deformation and strain distributions of bulged tubes in the FHB experiments

$$F_f = \mu P \pi (2r_0 - t)(L - l) \quad (19)$$

(4) **Hi-speed DIC system.** The system is a non-contact optical real-time data acquisition system for 3D deformation and strain distributions of physical samples under static or dynamic loads. The system is consisted of two charge-coupled-device (CCD) cameras, several light-emitting diode (LED) lights, a control box, a computer, and a tripod, as shown in Fig. 7. Prior to the bulging, tubular blanks were sprayed with two kinds of paints to form irregular black speckles on a white background. During the process, the speckle images in the bulging zone of the tube were captured in real-time by the two high-speed CCD cameras (with a maximum frame rate of 340 frames per second). The captured speckle images were then analysed and processed by the software of the hi-speed DIC system. Finally, the deformation data required for the establishment of the equivalent stress-strain relationship, including the instantaneous coordinates, strains, wall thickness, etc., were obtained from the analysed and processed speckle images.

4.2 Experimental method

SS304 stainless steel tubes were adopted in the present FHB experiments. The geometric and mechanical parameters of the tubular blanks are listed in Table 1.

Table 1 Geometric and mechanical parameters of SS304 stainless steel tubes adopted in the experiments

Geometric parameters	Values	Mechanical parameters	Values
Initial wall thickness t_0 (mm)	0.6	Tensile strength σ_b (MPa)	654
Initial outer diameter D_0 (mm)	32	Yield strength σ_s (MPa)	410
Initial length L (mm)	110	Strength coefficient K (MPa)	1349.2
Bulged length l (mm)	50	Strain hardening index n (-)	0.2876

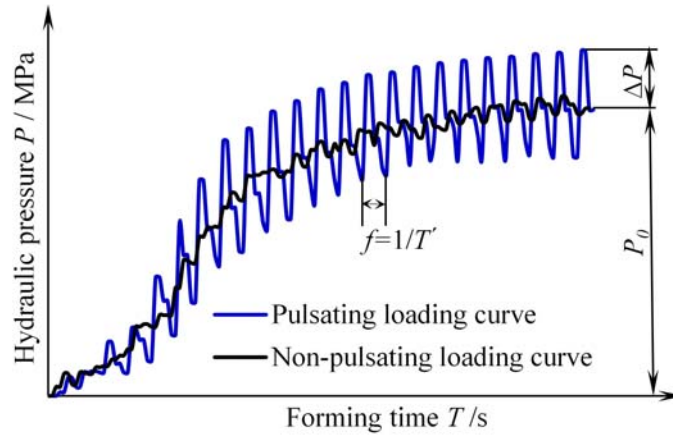


Fig. 8 Two typical pulsating loading curves adopted in the presented experiments

The FHB experiments were performed on the custom-made THF experimental system. Two typical pulsating loading paths were adopted in the present experiments, as shown in Fig. 8, including pulsating curve (with increased fluctuation) and non-pulsating curve (with minor fluctuation).

The experimental procedures of the FHB experiments are described next. Both the hydraulic power generation system and the pulsation generation system were kept running in order to generate a pulsating hydraulic pressure $P = P_0 + \Delta P \sin(2\pi fT)$ in the hydraulic chamber. The pulsating hydraulic fluid was then supplied to the tubular blank on the FHB device, as shown in Fig. 6, where the pulsating FHB of the tube was generated. During the bulging, the median hydraulic pressure P_0 and the pulsating hydraulic pressure P values were recorded by the two pressure transducers every 0.1 s. These values were stored by the paperless recorder from which the hydraulic pressure curve can be output. The deformation images of the bulged tubes at each time step were captured in real-time and processed by the hi-speed DIC system, and 3D deformation and strain distributions on the bulging zone at each time step in the deformation process were then obtained.

The pulsating loading curve is similar to a sine curve despite its minor fluctuation, and can be approximately expressed as

$$P = P_0 + \Delta P \sin(2\pi fT) \quad (20)$$

where ΔP is the pulsation amplitude representing the average value of deviations between the peak and valley of the pulsating loading curve, f is the pulsation frequency defined by $f = 1/T'$, where T'

is the pulsation cycle of the pulsating loading curve.

Both ΔP and f were calculated based on the data recorded by the pressure transducers. The pulsation frequency and amplitude of the hydraulic pressures could be changed by presetting the stroke and speed of the slider of the servo press. The pulsation amplitudes of 2.77 MPa, 3.34 MPa, 3.92 MPa, and 4.95 MPa, and the pulsating frequencies of 1.3 Hz, 1.7 Hz, 2.1 Hz, and 2.5 Hz were adopted in the experiments.

On the other hand, when the piston rod of the pulsation generation system was kept still, the fluid from the hydraulic power generation system was directly led into the tubular blank on the FHB device. Thus, the tube was bulged under a monotonically increasing hydraulic pressure P_0 and a non-pulsating FHB was realised.

5. Results and discussion

In this section, equivalent stress-strain relationships determined based on the experimental and simulation results of pulsating and non-pulsating FHB are compared to verify the proposed method in this paper. Correspondingly, the effects of the pulsation amplitude and frequency on the equivalent stress-strain curves determined based on the experimental deformation data are analysed.

5.1 Comparison of the equivalent stress-strain curves

5.1.1 The equivalent stress-strain curves based on the experimental data

After the deformation data were generated, including the instantaneous coordinates, strains, wall thickness, and other data parameters, obtained by the hi-speed DIC system, these were substituted into the calculation formulas derived in Section 3, and the values of equivalent stresses and strains of the tubes under pulsating and non-pulsating FHB were obtained, as shown in Fig. 9. As also shown in Fig. 9, the actual equivalent stress-strain curves change in a pulsating manner under the pulsating hydraulic pressures, and the fluctuation becomes distinct with the increase of the pulsation amplitude.

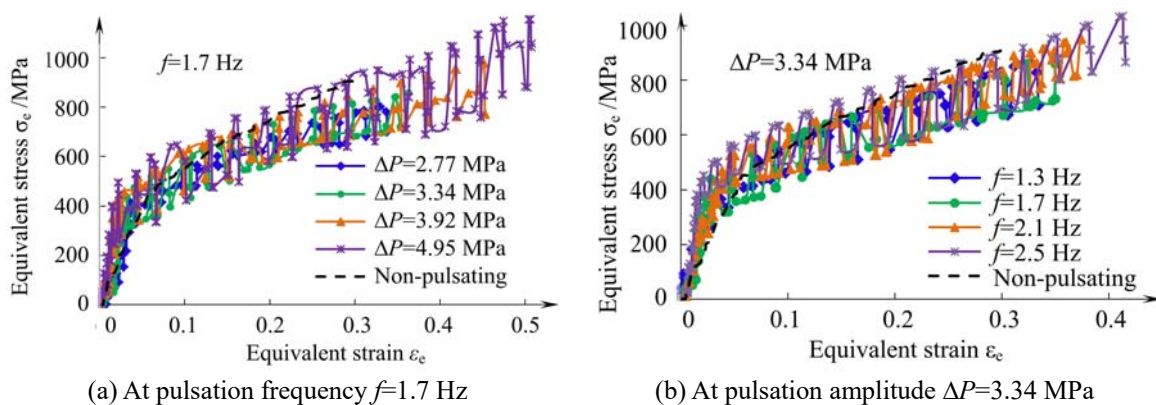


Fig. 9 The actual equivalent stress-strain curves of tubes in free hydraulic bulging experiments under various pulsation amplitudes

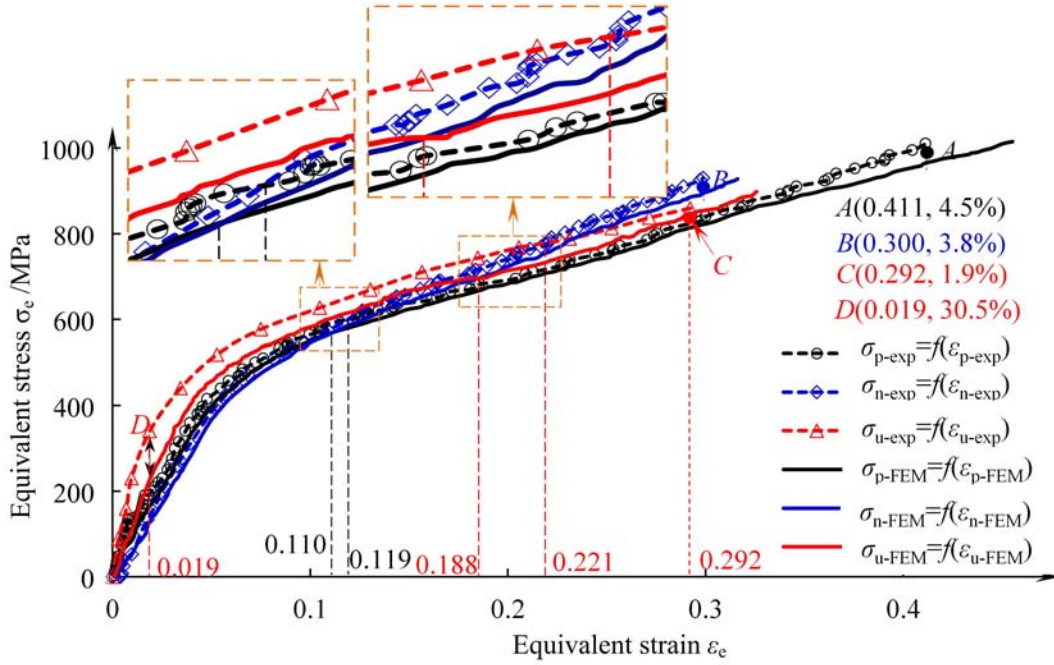


Fig. 10 Equivalent stress-strain relationships of the tubes obtained based on the experimental data and the simulation data

Table 2 Equivalent stress-strain relationships of tubes obtained based on the experimental data

Experiments	Curve-fitting methods	Equivalent stress-strain relationships
Pulsating hydroforming	Polynomial formula (21)	$\sigma = 562941\varepsilon^5 - 764492\varepsilon^4 + 395539\varepsilon^3 - 95471\varepsilon^2 + 118 + 64\varepsilon + 13.657$
Non-pulsating hydroforming	Polynomial formula (21)	$\sigma = 626223\varepsilon^5 - 821306\varepsilon^4 + 401090\varepsilon^3 - 92902\varepsilon^2 + 12045\varepsilon - 37.73$
Uniaxial tensile test	Hollomon formula $\sigma = K\varepsilon^n$	$\sigma = 1349.2\varepsilon^{0.2876}$

For the convenience of comparison, the coordinates at the peaks of the actual equivalent stress-strain curves were extracted and fitted with the polynomial formula (Eq. (18)) and the Hollomon formula $\sigma = K\varepsilon^n$ with the use of UTT. Thus, three equivalent stress-strain curves were obtained, as indicated by the set of dotted lines in Fig. 10. The equivalent stress-strain relationships obtained by curve-fitting the experimental data are shown in Table 2. As shown in Fig. 10, the values of the equivalent stress-strain curve $\sigma_{u-exp} = f(\varepsilon_{u-exp})$ based on UTT is the highest, followed by the equivalent stress-strain curve $\sigma_{p-exp} = f(\varepsilon_{p-exp})$ of the pulsating FHB at strain values $\varepsilon_e < 0.119$. The latter is slightly higher than the equivalent stress-strain curve $\sigma_{n-exp} = f(\varepsilon_{n-exp})$ of the non-pulsating FHB. The equivalent stress-strain curve $\sigma_{n-exp} = f(\varepsilon_{n-exp})$ of the non-pulsating FHB exceeds the curve $\sigma_{p-exp} = f(\varepsilon_{p-exp})$ of the pulsating FHB at strain values $\varepsilon_e \geq 0.119$ and the UTT curve $\sigma_{u-exp} = f(\varepsilon_{u-exp})$ at strain values $\varepsilon_e \geq 0.221$. In addition, the limit equivalent strain at the bursting moment of the tube of pulsating FHB is largest (at point A), followed by that of the non-pulsating FHB (at point B). Additionally, the limit equivalent strain of UTT is smallest (at point C). As a result, different loading schemes elicit different equivalent stress-strain curves of tubes and larger deformation can

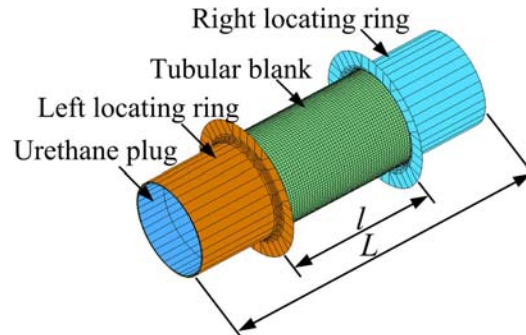


Fig. 11 Finite element model for the FHB

be obtained by hydroforming rather than by uniaxial tensile, or by pulsating FHB rather than by non-pulsating FHB.

5.1.2 Equivalent stress-strain curves derived based on the simulation data

An FE model for FHB was established based on the use of the FHB device, as shown in Fig. 11. The geometric parameters, deformation conditions, and loading curves adopted in the FE simulation were consistent with those elicited in the experiments of FHB. The tubular material is assumed to be homogeneous, isotropic, and incompressible, and meets the von Mises yield criterion. The locating rings and urethane plugs are modelled as rigid elements. The initial gap between the locating rings and the urethane plugs was set to be the initial wall thickness, t_0 , of the tubular blanks. The contact interactions between the tubular blank and the dies were modelled using Coulomb's law with a constant friction coefficient of 0.125, which was identical in value to that in the FHB experiments (Yang *et al.* 2008).

After the equivalent stress-strain curves of $\sigma_{p-exp}=f(\varepsilon_{p-exp})$ and $\sigma_{n-exp}=f(\varepsilon_{n-exp})$ were generated, which were obtained based on pulsating and non-pulsating FHB experiments, these were input into the FE model as respective material models. FE simulations of pulsating and non-pulsating FHB were then carried out. The equivalent stress-strain curve of $\sigma_{u-exp}=f(\varepsilon_{u-exp})$ was then input into the FE model as a material model, and FE simulations of non-pulsating hydroforming were carried out. The FE simulations were carried out using the software Dynaform. The values of the coordinates, axial, and circumferential strains, and instantaneous wall thickness of the bulged profiles, were then drawn out from the three FE simulation results. They were subsequently substituted into the calculation formulas listed in Section 3. Finally, the equivalent stress-strain curves $\sigma_{p-FEM}=f(\varepsilon_{p-FEM})$, $\sigma_{n-FEM}=f(\varepsilon_{n-FEM})$, and $\sigma_{u-FEM}=f(\varepsilon_{u-FEM})$, were determined based on the simulation data, as a set of solid lines indicated in Fig. 10.

As shown in Fig. 10, the values of the equivalent stress-strain curve $\sigma_{u-FEM}=f(\varepsilon_{u-FEM})$ based on the use of UTT data as the material model in the FE simulations is the highest, followed by the equivalent stress-strain curve $\sigma_{p-FEM}=f(\varepsilon_{p-FEM})$ with pulsating experimental data as the material model in FE simulations for strains $\varepsilon_e < 0.110$. The latter is slightly higher in values than the equivalent stress-strain curve $\sigma_{n-FEM}=f(\varepsilon_{n-FEM})$ with the non-pulsating experimental data used as the material model in the FE simulations. The equivalent stress-strain curve $\sigma_{n-FEM}=f(\varepsilon_{n-FEM})$ surpasses both the curve $\sigma_{p-FEM}=f(\varepsilon_{p-FEM})$ for strains $\varepsilon_e \geq 0.110$ and the curve $\sigma_{u-exp}=f(\varepsilon_{u-exp})$ for strains $\varepsilon_e \geq 0.188$. It is obvious that behaviours of the equivalent stress-strain curves obtained based on the simulation data basically coincided with those obtained based on the experimental data.

5.1.3 Discrepancy between the experimental and FE simulation-derived equivalent stress-strain curves

It is observed in Fig. 10 that the equivalent stress-strain curves based on the experimental data are higher than those curves based on the simulation data, although some degree of discrepancy was observed as indicated next.

- For the FE simulation of the non-pulsating FHB with $\sigma_{u-exp}=f(\varepsilon_{u-exp})$ as the material model, which is based on UTT data, the largest discrepancy between its resulting curve $\sigma_{u-FEM}=f(\varepsilon_{u-FEM})$ and input curve $\sigma_{u-exp}=f(\varepsilon_{u-exp})$ is approximately 30.5% (the discrepancy is calculated using the equation $|\sigma_{FE}-\sigma_{test}|/\sigma_{test}\times 100\%$) and occurs at point *D* at the initial stage ($\varepsilon_e=0.019$) of the deformation.
- For the FE simulation of the non-pulsating FHB with $\sigma_{n-exp}=f(\varepsilon_{n-exp})$ as the material model, which is based on non-pulsating FHB experiment data, the largest discrepancy between its resulting curve $\sigma_{n-FEM}=f(\varepsilon_{n-FEM})$ and input curve $\sigma_{n-exp}=f(\varepsilon_{n-exp})$ is approximately 3.8% and occurs at point *B* at the late stage ($\varepsilon_e=0.300$) of the deformation.
- For the FE simulation of the pulsating FHB with $\sigma_{p-exp}=f(\varepsilon_{p-exp})$ as the material model, which is based on pulsating FHB experiment data, the largest discrepancy between its resulting curve $\sigma_{p-FEM}=f(\varepsilon_{p-FEM})$ and the input curve $\sigma_{p-exp}=f(\varepsilon_{p-exp})$ is approximately 4.5% and occurs at point *A* at the late stage ($\varepsilon_e=0.411$) of the deformation.

Based on the analyses described above, it is quite clear that the FE simulation of FHB with the equivalent stress-strain relationship obtained based on the FHB experiment data as the input material model, produce higher precision than those elicited using the material model based on data from UTT.

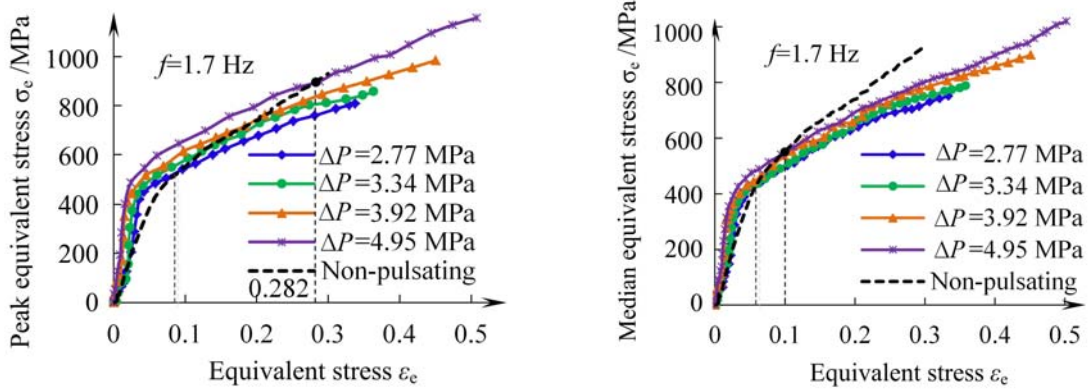
5.2 Effect of pulsating parameters on the equivalent stress-strain curves

By comparing the equivalent stress-strain curves determined based on the experimental data, it was found that the pulsation amplitudes and frequencies had similar effects on the equivalent stress-strain curves. Therefore, the experimental results under pulsation frequency $f=1.7$ Hz and pulsation amplitude $\Delta P=3.34$ MPa were singled out to demonstrate the effect.

5.2.1 Effect of pulsation amplitudes on the equivalent stress-strain curves

In order to clearly demonstrate the effect of pulsation amplitude on the equivalent stress-strain curves, the peak and median equivalent stress-strain curves, which were based on the peak and median data of the equivalent stress-strain curves in Fig. 9(a), were respectively plotted in Fig. 12.

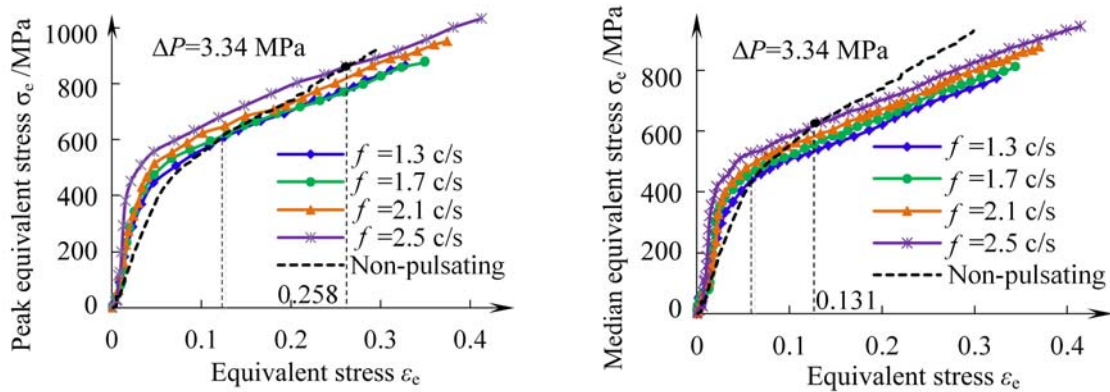
From Fig. 7 and Eq. (20), it is noted that the curve of the pulsating hydraulic pressure P oscillates about the median hydraulic pressure P_0 , and its pulsation amplitude increases gradually and stabilises at a certain forming time. A higher pulsating hydraulic pressure P generates a higher peak (or effective) hydraulic pressure P_{max} , which in turn creates a higher equivalent stress in pulsating hydroforming. Therefore, one could comprehend that peak and median equivalent stress-strain curves under pulsating FHB attain larger values with the increase of pulsation amplitudes. However, the equivalent stress-strain curves under non-pulsating FHB ascend fast and surpass those under pulsating FHB soon after the deformation, as indicated by the dotted lines in Fig. 12. One can see from Fig. 12 that the limit (maximum) equivalent strains at bursting in pulsating FHB increase with the pulsation amplitudes, and are larger than the limit equivalent strain in non-pulsating FHB. This implies that the formability of THF could be improved by the use of larger pulsating amplitude.



(a) Peak equivalent stress-strain curves

(b) Median equivalent stress-strain curves

Fig. 12 Equivalent stress-strain curves of tubes in FHB experiments under pulsation frequency $f=1.7$ Hz



(a) Peak equivalent stress-strain curves

(b) Median equivalent stress-strain curves

Fig. 13 Equivalent stress-strain curves of tubes in FHB experiments under pulsation amplitude $\Delta P=3.34$ MPa

5.2.2 Effect of pulsation frequency on the equivalent stress-strain curves

The effect of pulsation frequency on the equivalent stress-strain curve is similar to that of the pulsation amplitude, as illustrated in Fig. 13. The peak and median equivalent stress-strain curves under pulsating FHB become higher with the increase of pulsation frequency, but the equivalent stress-strain curves under non-pulsating FHB ascend fast and surpass those under pulsating FHB soon after the deformation, as indicated by the dotted lines in Fig. 13. One can see from Fig. 13 that the limit equivalent strains at bursting in pulsating FHB increase with the pulsation frequency, and are larger than the limit equivalent strain in non-pulsating FHB. This implies that the formability of hydroforming of tubes could be improved by a higher pulsation frequency.

5. Conclusions

In this paper, the equivalent stress-strain curves of tubes in pulsating and non-pulsating

hydroforming were determined and compared based on FHB experiments and FE simulation data, and the effect of the pulsation amplitude and frequency on these curves was analysed. The following conclusions can be drawn from the study:

- A method to determine the equivalent stress-strain relationship of tubes in pulsating hydroforming is proposed based on the mechanical model of FHB, incremental plasticity theory, the law of plastic deformation work, and the use of a fitting method and FHB experiments, based on the assumption that the bulged profiles and equivalent stress-strain relationship can be described by polynomial formulas. Using the proposed method, the equivalent stress-strain relationship can be obtained without on-line measurement of the instantaneous meridian radii of the bulged profiles as performed usually. Additionally, the deformation behaviours of tubes in pulsating THF can be well described by the resultant equivalent stress-strain relationship
- The FE simulation of THF in combination with the equivalent stress-strain relationship obtained based on the data from THF experiments used as an input material model produces higher precision results than those elicited using the material model, based on data from UTT
- The actual equivalent stress-strain curves for pulsating THF changes in an oscillatory way under various pulsation amplitudes and frequencies, and the fluctuation becomes distinct with the increase of the pulsation amplitude and frequency
- The equivalent stress-strain curves under pulsating THF increase in magnitude with the increase of pulsation amplitude and frequency, but the equivalent stress-strain curves under non-pulsating THF ascend fast and surpass those under pulsating THF soon after the deformation
- The limiting equivalent strains at burst in pulsating THF increase with the pulsation amplitude and frequency, and are larger than the limit equivalent strain in non-pulsating THF. This implies that the formability of THF could be improved by a larger pulsating amplitude and a higher pulsation frequency.

Acknowledgments

The authors gratefully acknowledge the support of the National Natural Science Foundation of China (grant number 51271062), Guangxi Natural Science Foundation (grant number 2013GXNF0019305) and Innovation Project of Guilin University of Electronic Technology Graduate Education (GDYCSZ201401).

References

- Bortot, P., Ceretti, E. and Giardini, C. (2008), "The determination of flow stress of tubular material for hydroforming applications", *J. Mater. Proc. Tech.*, **203**(1-3), 318-388.
- Boudeau, N. and Malécot, P. (2012), "A simplified analytical model for post-processing experimental results from tube bulging test: Theory, experimentations, simulations", *Int. J. Mech. Sci.*, **65**, 1-11.
- Fuchizawa, S. and Narazakiv, M. (1993), "Bulge test for determining stress-strain characteristics of thin tubes", *Adv. Tech. Plast.*, **1**, 488-493.
- Hosford, W.F. and Caddell R.M. (2011), *Plasticity Metal Forming: Mechanics and Metallurgy*, 3rd Edition, W.F. Hosford, Ed., Cambridge University Press, USA.
- Hwang, Y.M. and Wang, C.W. (2009), "Flow stress evaluation of zinc copper and carbon steel tubes by

- hydraulic bulge tests considering their anisotropy”, *J. Mater. Proc. Tech.*, **209**(9), 4423-4428.
- Jia, H.J., Yang, L.F. and Liu, J.W. (2014), “Establishment of stress-strain relationships of tailor-welded tubes via DIC method based on uniaxial tensile tests”, *Key Eng. Mater.*, **611-612**, 475-482.
- Loh-Mousavi, M., Bakhshi-Jooybari, M., Mori, K. and Hyashi, K. (2008), “Improvement of formability in T-shape hydro-forming of tubes by pulsating pressure”, *Eng. Manuf.*, **222**, 1139-1146.
- Loh-Mousavi, M., Bakhshi, M. and Mori, K. (2010), “Mechanism of improvement of formability in pulsating hydroforming of T-shape tubes”, *Amirkabir/MISC*, **42**(1), 29-35.
- Loh-Mousavi, M., Bakhshi, M., Mori, K., Maeno, T., Farzin, M. and Hosseinipour, S.J. (2008), “3-D finite element simulation of pulsating free bulge hydroforming of tubes”, *Iran. J. Sci. Technol. B*, **32**(6), 611-618.
- Loh-Mousavi, M., Mirhosseini, A.M. and Amirian, G. (2011), “Investigation of modified bi-layered tube hydro-forming by pulsating pressure”, *Key Eng. Mater.*, **15**(486), 5-8.
- Mori, K., Maeno, T. and Maki, S. (2007), “Mechanism of improvement of formability in pulsating hydroforming of tubes”, *Int. J. Mach. Tool. Manuf.*, **47**(6), 978-984.
- Rikimaru, T. and Ito, M. (2001), “Hammering hydro-forming of tubes”, *Press Work.*, **39**(7), 58-65.
- Strano, M. and Altan, T. (2004), “An inverse energy approach to determine the flow stress of tubular materials for hydroforming applications”, *J. Mater. Proc. Tech.*, **146**(1), 92-96.
- Xu, Y., Zhang, S.H., Cheng, M., Song, H.W. and Zhang, X.S. (2014), “Application of pulsating hydroforming in manufacture of engine cradle of austenitic stainless steel”, *Procedia. Eng.*, **81**, 2205-2210.
- Yang, L.F. and Guo, C. (2008), “Determination of stress-strain relationship of tubular material with hydraulic bulge test”, *Thin Wall. Struct.*, **46**, 147-154.
- Yang, L.F., Rong, H.S. and He, Y.L. (2014), “Deformation behavior of a thin-walled tube in hydroforming with radial crushing under pulsating hydraulic pressure”, *J. Mater. Eng. Perform.*, **23**(2), 429-438.
- Zhan, M., Du, H.F., Liu, J., Ren, N., Yang, H., Jiang, H.M., Diao, K.S. and Chen, X.P. (2010), “A method for establishing the plastic constitutive relationship of the weld bead and heat-affected zone of welded tubes based on the rule of mixtures and a micro-hardness test”, *Mater. Sci. and Eng.*, **527**, 2864-2874.

CC

Nomenclature

σ_e (MPa)	Equivalent stress, Eq. (16)
ε_e (-)	Equivalent strain, Eq. (15)
σ_φ (MPa)	Meridian stress on the bulged profile, Fig. 3
σ_θ (MPa)	Circumferential stress of the bulged profile, Fig. 3
σ_t (MPa)	Thickness stress of the bulged profile
$d\varepsilon_{\varphi(i)}$ (-)	Meridian strain increment any time step (i) in FHB process, Eq. (13)
$d\varepsilon_{\theta(i)}$ (-)	Circumferential strain increment at any time step (i) in FHB process, Eq. (13)
$d\varepsilon_{t(i)}$ (-)	Thickness strain increment at any time step (i) in FHB process, Eq. (13)
t_0 (mm)	Initial wall thickness of tubular blanks, Fig. 2(a) and Table 1
r_0 (mm)	Initial outer radius of tubular blanks, Fig. 2(a)
L (mm)	Initial length of tubular blanks, Fig. 2(a) and Table 1
l (mm)	Bulged length of the free-bulged zone, Fig. 2(a)
a, b, c, d	Four points of infinitesimal element S on the bulged profile, Fig. 3(a)
$y, f(z)$ (mm)	Hypothesized polynomial functions used to express the bulged profiles, Fig. 2 and Eq. (10)

j (-)	Any point on the bulged profile, Fig. 2(b)
p	Peak point on the bulged profile, Fig. 3(c)
$\rho_{\phi a}, \rho_{\phi b}$ (mm)	Median radii of the points a and b on the longitudinal (axial) profile, respectively, Fig. 3
$\rho_{\theta a}, \rho_{\theta b}$ (mm)	Circumferential radii of the points a and b on the transverse cross-section, respectively, Fig. 3
t (mm)	Instantaneous wall thickness of any point on the bulged profile, Fig. 2(b)
\overline{ab}_{in} (mm)	Length of inner arc between points a and b of infinitesimal element S on the bulged profile, Fig. 3
\overline{ab}_{mid} (mm)	Length of middle arc between points a and b of infinitesimal element S on the bulged profile, Fig. 3
t_a, t_b (mm)	Wall thicknesses of the points a and b on the bulged profile, Fig. 3(a)
t_p (mm)	Average wall thickness of peak point p on the bulged profile, $t_p=(t_a+t_b)/2$, Fig. 3(c).
ϕ_a, ϕ_b (°)	Angle between tangents of the points a and b on the longitudinal (axial) profile and the z- axis, Fig. 3(c)
φ (°)	Angle between the median radii of the points a and b on the longitudinal (axial) cross-section
γ (°)	Angle between the straight line ab on the bulged profile and the z-axis, Fig. 3(c)
θ (°)	Angle between median radii of the points a and b on the transverse cross-section, Fig. 3(b)
P_0 (MPa)	Median hydraulic pressure non-pulsating FHB, Eq. (20)
P (MPa)	Pulsating hydraulic pressure in pulsating FHB, Eq. (20)
F_f (N)	Friction between tube and dies, Fig. 2(b) and Eq. (3)
ΔP (MPa)	Pulsation amplitude of the hydraulic pressure, Fig. 8 and Eq. (20)
f (Hz)	Pulsation frequency of the hydraulic pressure, Fig. 8 and Eq. (20)
T (s)	Pulsation cycle of the hydraulic pressure, Fig. 8
T (s)	Forming time in THF, Fig. 8
i (s)	Time step (i) in the FHB process, Fig. 1 and Eq. (13)